

This version of the article has been accepted for publication, after peer review (when applicable) and is subject to Springer Nature's AM terms of use (<https://www.springernature.com/gp/open-research/policies/accepted-manuscript-terms>), but is not the Version of Record and does not reflect post-acceptance improvements, or any corrections. The Version of Record is available online at: <http://dx.doi.org/10.1007/s11440-021-01140-w>.

1
2
3 **CONSTRUCTION OF SOIL-WATER CHARACTERISTIC CURVE OF**
4 **GRANULAR MATERIALS WITH TOROIDAL MODEL AND**
5 **ARTIFICIALLY GENERATED PACKINGS**

6 Bate, Bate, A.M. ASCE
7
8

“100-Talents Program” Professor, Institute of Geotechnical Engineering, College of Civil
Engineering and Architecture, MOE Key Laboratory of Soft Soils and Geoenvironmental
Engineering, Zhejiang University, China

9
10 Nie, Shaokai
11
12

Graduate Research Assistant, Institute of Geotechnical Engineering, College of Civil
Engineering and Architecture, MOE Key Laboratory of Soft Soils and Geoenvironmental
Engineering, Zhejiang University, China

13
14 Chen, Zejian*
15
16

Graduate Research Assistant, The Hong Kong Polytechnic University, Hong Kong SAR;
Formerly, Undergraduate Research Assistant, Institute of Geotechnical Engineering, College of
Civil Engineering and Architecture, MOE Key Laboratory of Soft Soils and Geoenvironmental
Engineering, Zhejiang University

17 Email address: ze-jian.chen@connect.polyu.hk
18
19

20
21 Zhang, Fengshou
22
23

Professor, Department of Geotechnical Engineering, College of Civil Engineering, Tongji
University, China

24
25 and
26
27
28

29 Chen, Yunmin
30
31

Academician of CAS, Professor, Institute of Geotechnical Engineering, College of Civil
Engineering and Architecture, MOE Key Laboratory of Soft Soils and Geoenvironmental
Engineering, Zhejiang University, China

32
33
34
35
36
37
38 (Accepted Version of DOI:[10.1007/s11440-021-01140-w](http://dx.doi.org/10.1007/s11440-021-01140-w))
39
40

1 **Construction of Soil-Water Characteristic Curve of Granular Materials with Toroidal**
2 **Model and Artificially Generated Packings**
3

4 **Abstract** The soil-water characteristic curve (SWCC) of granular materials is crucial for many
5 emerging engineering applications, such as permeable pavement and methane hydrate extraction.
6 Laboratory determination of the SWCC of granular materials suffers from inaccurate volume
7 readings by the diffused air bubbles in the hanging column and sudden desaturation at small matric
8 suction intervals. Theoretical determination of the SWCC of granular materials also suffers from
9 semi-empirical nature in the prediction from grain size distribution, or from the limitation of
10 assumed cubic packing or face-centered cubic packing with a toroid meniscus water model. In this
11 study, real three-dimensional particle packing was first rendered with the discrete element method
12 using approximation of spheres. Then, the Young-Laplace equation was applied to calculate the
13 volume of toroidal meniscus water between each pair of spheres, which adds to the water content
14 in the pendular regime of the SWCC. Additionally, a digitized image algorithm was used to
15 identify the pore throats and calculate the air entry value and residual matric suction, the
16 connection of which yields a straight line approximating the funicular regime. The SWCC was
17 thus constructed. Comparison with laboratory measured SWCCs suggested that although
18 reasonable agreement was reached in general for glass beads, residual water content was
19 underestimated especially for non-spherical granular materials. Several possible reasons were
20 discussed including the existence of patchy water accounting for the major portion of water in the
21 beginning of pendular regime of granular materials, which was also observed in microscopic
22 photos through a special desaturation experiment.

23 **Keywords:** soil-water characteristic curve, granular materials, packing, toroidal model, discrete
24 element method.

25 **1 Introduction**

26 The soil-water characteristic curve (SWCC) of granular materials is a crucial property for
27 many emerging engineering applications, such as permeable pavement, geotechnical structures
28 made of construction and demolished wastes, ocean methane hydrate extraction, and CO₂
29 imbibition in enhanced oil recovery. Comprising a relationship between matric suction and water

30 content, SWCC characterizes the key properties of unsaturated soil and can be used to derive many
31 mechanical properties including shear strength, stiffness, consolidation, and hydraulic
32 conductivity (Fredlund et al. 1978; Lu et al. 2009; Lu et al. 2008; Fredlund et al. 2012; Gens 1996;
33 Sheng and Zhou 2010; Zhang and Lytton 2008). Matric suction Ψ , originating from meniscus
34 water (Fredlund and Rahardjo 1993), is the difference of air pressure and pore water pressure (i.e.
35 $u_a - u_w$). Laboratory determination of SWCC of granular materials often involves a hanging
36 column. The accuracy of the measured SWCC suffers from diffused air bubbles in the volume
37 reading in the hanging column and sudden desaturation at small matric suction values. Semi-
38 empirical formulas were also used in predicting the SWCC from grain size distribution (e.g.
39 Fredlund and Xing 1994; van Genuchten 1980), while the physical meanings of the associated
40 fitting parameters are mostly unclear.

41 There are four regimes in the SWCC, namely: (1) saturated regime (saturated with non-
42 negative pore water pressure); (2) capillary regime (saturated with negative pore water pressure);
43 (3) funicular regime (continuous water and air phases with matric suction $>$ air entry value (AEV));
44 and (4) pendular regime (discontinuous water phase and continuous air phase) (Fredlund and
45 Rahardjo 1993; Fredlund 2006; Mitarai and Nori 2006). In pendular regime, water was perceived
46 to be mainly in the form of liquid bridges (meniscus toroid) and absorbed films (Leverson and
47 Lohnes 1995; Mason et al. 1999). The volume of meniscus toroid between a pair of ideal spherical
48 particles of different sizes under a given matric suction can be described by the Young-Laplace
49 equation (Fisher 1926; Orr et al. 1975; Lian et al. 1993; Lechman and Lu 2008). By combining the
50 solution with a certain particle packing, the macroscopic SWCC of granular materials can be
51 predicted. Two basic types of ideal particle packings, namely simple cubic packing and face-
52 centered packing are often built to simulate the loosest and densest situation respectively (Cho and

53 Santamarina 2001; He et al. 2010; Likos and Lu 2004; Cao et al. 2017). However, they fail to
54 represent an actual packing state. Therefore, actual particle size distribution and porosity were also
55 taken into consideration in recent mathematical simulations by establishing the distribution of pore
56 sizes (Likos and Jaafar 2013; Suits et al. 2011; Wan et al. 2018). Gan et al. (2013) adopted a
57 complicated particle–water discrete element method to investigate the hysteresis of SWCC with
58 considerations of real particle size distribution and random packing and achieved some reasonable
59 results. To date, successful and simple construction of SWCC of granular particles by directly
60 generating a real particle arrangement (e.g. by discrete element method) with definite theoretical
61 basis is still very limited.

62 The objective of this study is to propose a new method to predict the SWCC of granular
63 materials. The following tasks were carried out: (1) Generating a 3D rendition of spherical particles
64 at realistic porosity to simulate granular materials with discrete element method; (2) Employing
65 the Young-Laplace equation to calculate the volume of toroidal meniscus water between each pair
66 of spheres, which adds to the water content in the pendular regime of SWCC; (3) Using a digitized
67 image algorithm to simulate the connectivity of pores and calculate the air entry value and the
68 residual matric suction, which define the beginning and the end of the funicular regime. Through
69 the above steps, SWCC was constructed. Finally, the performance of the proposed SWCC model
70 was evaluated with comparisons of measured data and microscopic photos.

71

72 **2 Theoretical models for construction of SWCC in microscopic scale**

73 ***2.1 A numerical solution to Young-Laplace equation for the toroidal meniscus 74 model in the pendular regime***

75 Although granular materials are usually irregularly shaped, idealized spheres are used to
 76 simulate the particles in this study, which would greatly simplify the calculations. The toroidal
 77 meniscus model (also known as liquid bridge) [Fig.1(a)] is often used to delineate the water phase
 78 between adjacent particles in the pendular regime, usually with the following assumptions: gravity
 79 is neglected, particles are spheres, and water only resides in the meniscus toroid near the contact
 80 between each pair of spheres. The geometrical configuration of the meniscus toroid depends on
 81 surface tension (T_s) and matric suction $\Psi = (u_a - u_w)$ [Fig.1 (b)], which is described by the
 82 Young-Laplace equation:

$$(u_a - u_w) = T_s \cdot \left(\frac{1}{\rho_1} + \frac{1}{\rho_2} \right) \quad (1)$$

83 where ρ_1 and ρ_2 are the local curvature of the meniscus in orthogonal directions [Fig.
 84 1(b)]. The Young-Laplace equation is a second-order differential equation and its boundary
 85 conditions depend on liquid-solid contact angle, sphere radii and the gap between spheres. Many
 86 of the previous studies used circle approximation to solve the Young-Laplace equation, in which
 87 the curvature radius ρ_1 is considered constant. This approximation leads to a constant value of
 88 ρ_2 , which disagrees with the reality and results in errors especially for spheres with different sizes,
 89 as pointed out by some researchers (Lechman and Lu 2008; Lu et al. 2008).

90 Consequently, it is important to adopt the exact solution of the Young-Laplace equation in
 91 calculating the configuration of the meniscus toroid. As the meniscus is a rotational surface, Eq.(1)
 92 can be transformed into Eq. (2), under a coordination system established in Fig.1(c):

$$\frac{\Psi}{T_s} = 2H = \frac{1}{\rho_1} + \frac{1}{\rho_2} = \frac{\ddot{r}}{(\dot{r}^2 + 1)^{3/2}} - \frac{1}{r(\dot{r}^2 + 1)^{1/2}} \quad (2)$$

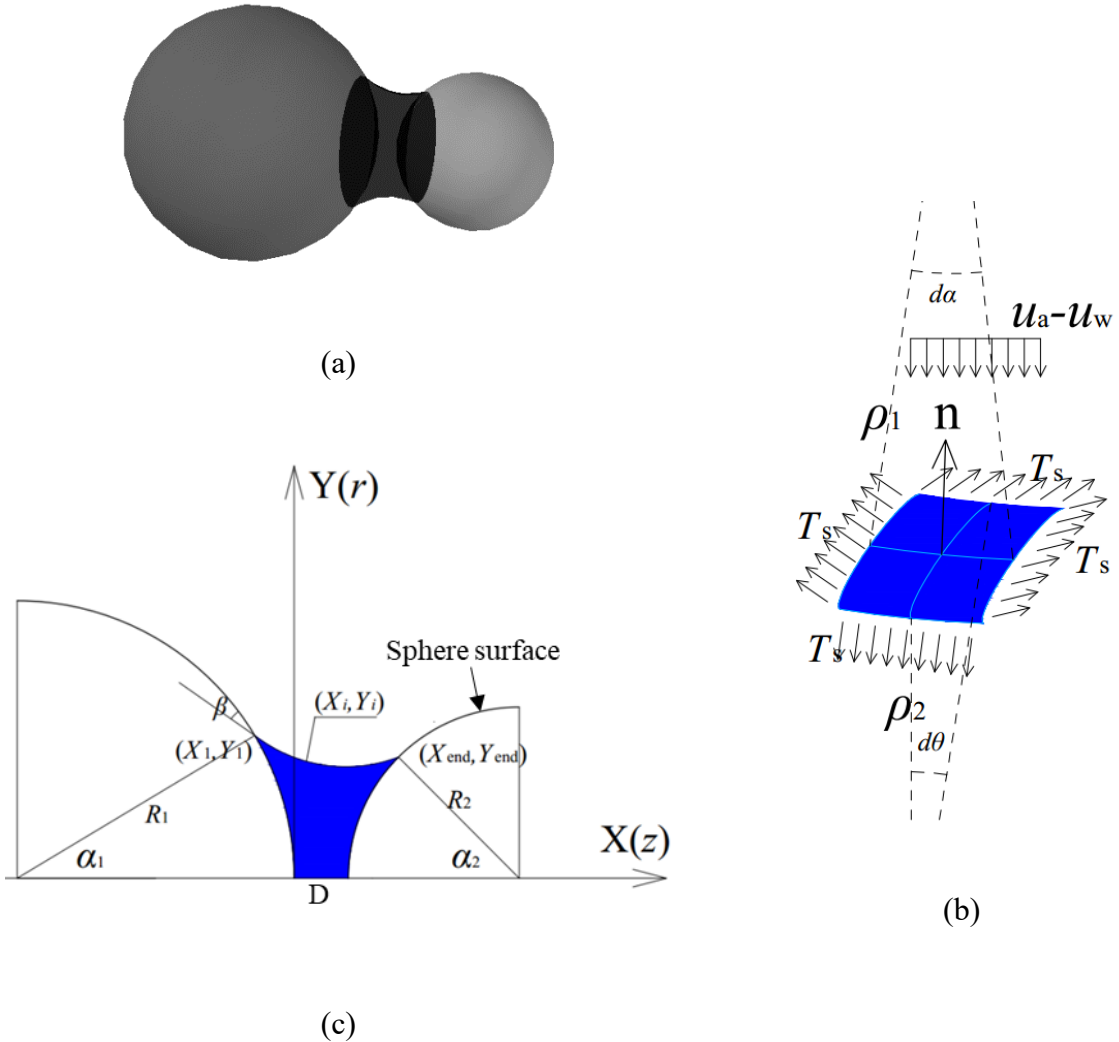
93 where H represents the mean curvature of the meniscus.

94

The boundary conditions can be written as follows:

$$\begin{cases} r|_{z=z_1} = R_1 \sin \alpha_1 & (a) \\ \dot{r}|_{z=z_1} = -\frac{1}{\tan(\alpha_1 + \beta)} & (b) \\ r|_{z=z_2} = R_2 \sin \alpha_2 & (c) \\ \dot{r}|_{z=z_2} = \frac{1}{\tan(\alpha_2 + \beta)} & (d) \end{cases} \quad (3)$$

95 Given matric suction Ψ , surface tension T_s , filling angles α_1, α_2 and contact angle β , the
 96 generatrix between two particles can be solved. However, as the filling angles are unknown, the
 97 analytical solutions are highly complicated and inconvenient to use (Orr et al. 1975). To address
 98 this problem, Lian et al. (1993) proposed a numerical solution for particle pairs with equal sizes
 99 based on the Euler method, which is extended in this study to consider arbitrary radii and inter-
 100 particle distance.



101 **Figure 1. Schematic diagrams of the meniscus toroid model: (a) A 3D diagram;**
 102 **(b) Diagram of force balance of an area element on the meniscus;**
 103 **(c) A plane-coordinate system for the numerical solution**

104 In Fig.1(c), (X_i, Y_i) describes a series of dense points on the meniscus toroid generatrix.

105 The values of Y_{i+1} at the point next to (X_i, Y_i) can be approximated by a second-order Taylor series:

$$Y_{i+1} = Y_i + \Delta X \cdot \dot{Y}_i + \frac{1}{2} \Delta X^2 \cdot \ddot{Y}_i \quad (4)$$

106 where $\dot{Y} = \frac{dY}{dX}$ and $\ddot{Y} = \frac{d^2Y}{dX^2}$.

107 Meanwhile, by making the substitution $Q = 1 + \dot{Y}^2$ (Lian et al. 1993), Eq. (2) can be
 108 simplified as Eq. (5):

$$\frac{dQ}{dY} - \frac{2Q}{Y} = 4HQ^{3/2} \quad (5)$$

109 where $\frac{dQ}{dY} = \frac{dQ}{dX} \frac{dX}{dY} = 2\dot{Y}\ddot{Y} \frac{1}{\dot{Y}} = 2\ddot{Y}$.

110 The solution of Eq. (5) is $\frac{Y}{Q^{1/2}} + HY^2 = C$, which can be written as Eq. (6):

$$\dot{Y}_i = \pm \left[\frac{Y_i^2}{(C - HY_i^2)^2} - 1 \right]^{1/2} \quad (6)$$

111 By rewriting Eq. (5), we have:

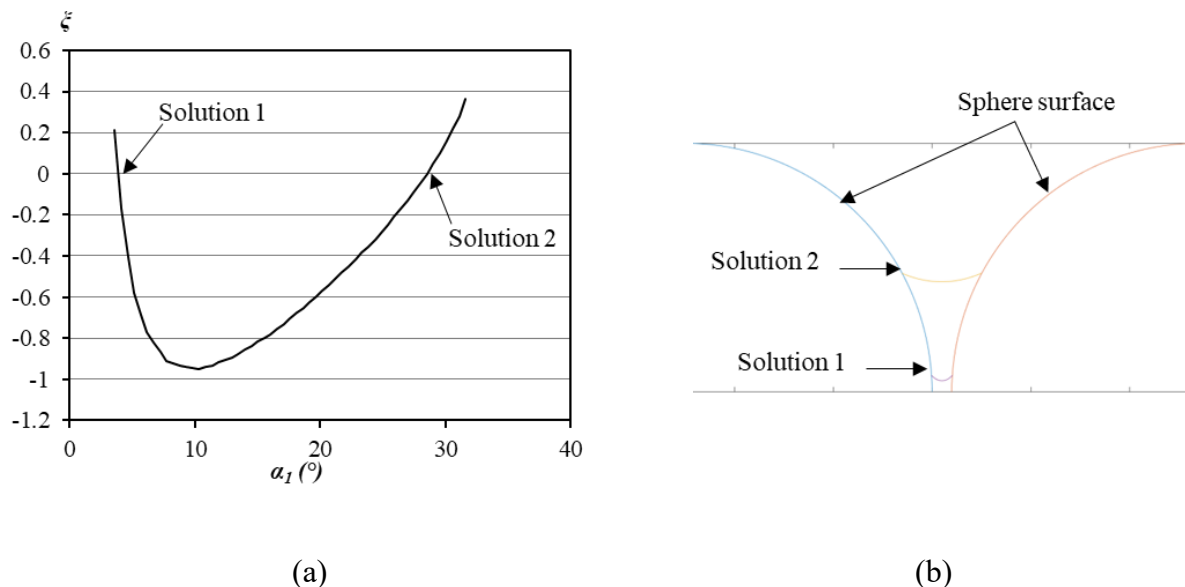
$$\ddot{Y}_i = \frac{1 + \dot{Y}_i^2}{Y_i} + 2H \left(1 + \dot{Y}_i^2 \right)^{3/2} \quad (7)$$

112 With Eqs. (4), (6) and (7) and boundary conditions (3), the configuration of the generatrix
 113 can be solved point by point. As long as the interval ΔX is sufficiently small, the accuracy of the
 114 solution will be ensured.

115 As shown in Fig. 1(c), the starting point (X_1, Y_1) on the generatrix curve is unknown,
 116 depending on the value of filling angle α_1 . Therefore, an iteration algorithm based on MATLAB
 117 was developed. This algorithm mainly includes four steps: (1) Set the filling angle at the bigger
 118 sphere as $\alpha_1 = \frac{\pi - \beta}{2} \cdot k$ (k varies from 1 to 1000), and obtain X_1 , Y_1 , \dot{Y}_1 , \ddot{Y}_1 and C based on
 119 geometric relationships and Eqs. (6)-(7); (2) Use Eq. (4) to extend the generatrix point by point,
 120 until it reaches the other sphere; (3) By looping k from 1 to 1000, different generatrix curves from
 121 different values of α_1 can be obtained; (4) Among these generatrix curves, the only one that best

122 fits all the boundary conditions will be selected as the true generatrix for the meniscus toroid
 123 between the two spheres.

124 With this algorithm, generatrix curve can be obtained with the given Ψ , T_s , β , R_1 , R_2
 125 and inter-particle gap D . It is worth noting that for non-contacting pairs of particles, there are two
 126 solutions under the same condition (Fig. 2). The generatrix curve with higher volume (i.e. higher
 127 α_1) was chosen as the exact solution to the Young-Laplace equation based on the minimum energy
 128 principle (Lian et al. 1993; Gras et al. 2011).



129 **Figure 2. Typical results of the algorithm. (a)** The value of ξ approaches zero twice as α_1
 130 increases; **(b)** The positions of two different generatrix solutions plotted in MATLAB as a
 131 result of (a). ($\xi = |\dot{Y}_{\text{end}} - \tan(\frac{\pi}{2} - \beta - \alpha_2)|$ is an index in the algorithm to evaluate the
 132 convergence of the solution. The lower ξ is, the better a solution fits the boundary conditions)
 133 After determination of the generatrix curve, toroid volume can be calculated accordingly.

134 First, the total volume surrounded by meniscus can be expressed as Eq. (8):

$$V = \sum \pi Y_i^2 \Delta X \quad (8)$$

135 Within the total volume, the solid part is calculated by the integral:

$$V_{cap1} = \frac{2\pi}{3} R_1^3 [1 - (\cos \alpha_1)^3] - \pi R_1^3 \cos \alpha_1 \sin \alpha_1 \quad (9)$$

$$V_{cap2} = \frac{2\pi}{3} R_2^3 [1 - (\cos \alpha_2)^3] - \pi R_2^3 \cos \alpha_2 \sin \alpha_2 \quad (10)$$

136

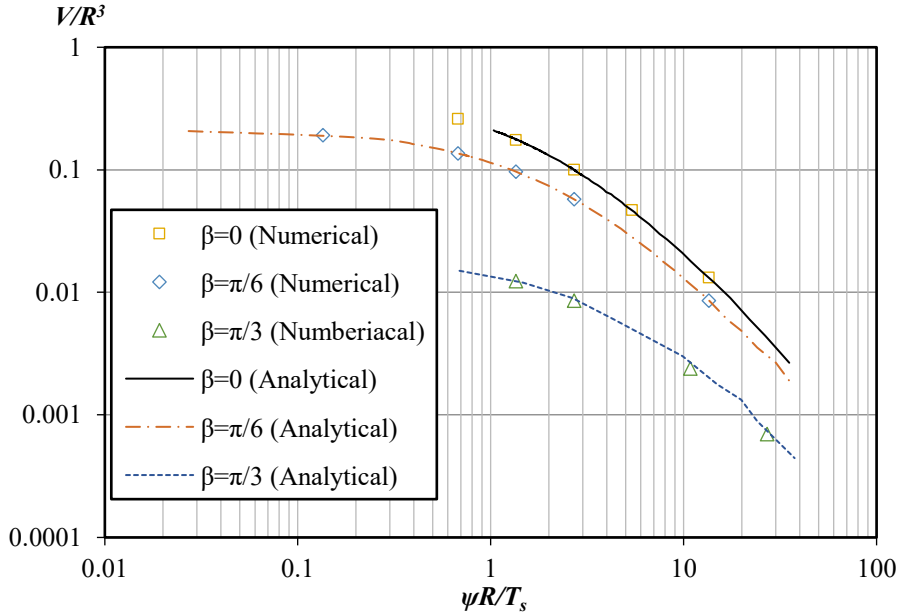
And the meniscus toroid volume is:

$$V_w = V - V_{cap1} - V_{cap2} \quad (11)$$

137

138

The results calculated by this method were almost identical to the data given in Lechman and Lu (2008) (Fig. 3), which was also verified by the tables provided by Orr et al. (1975).



139
140
141

Figure 3. Verification of the numerical solution in this study using the analytical solution in Lechman and Lu (2008), in which β is the contact angle, R is the radius of the spheres and V is the volume of the water

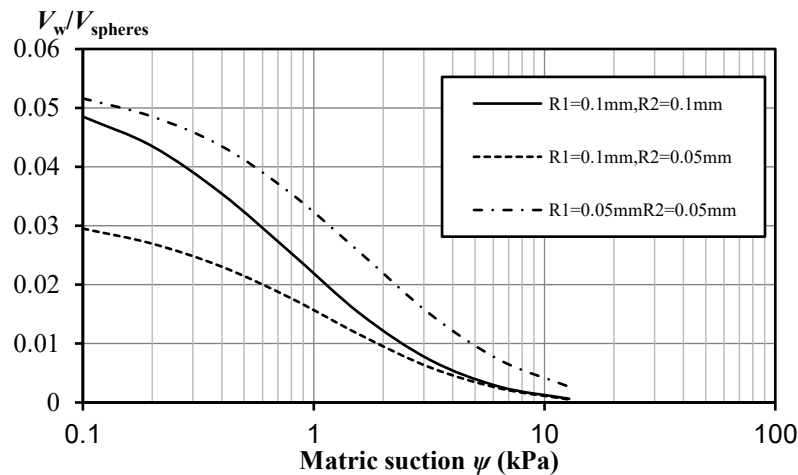
142

143

2.2 Influencing factors of the toroidal meniscus

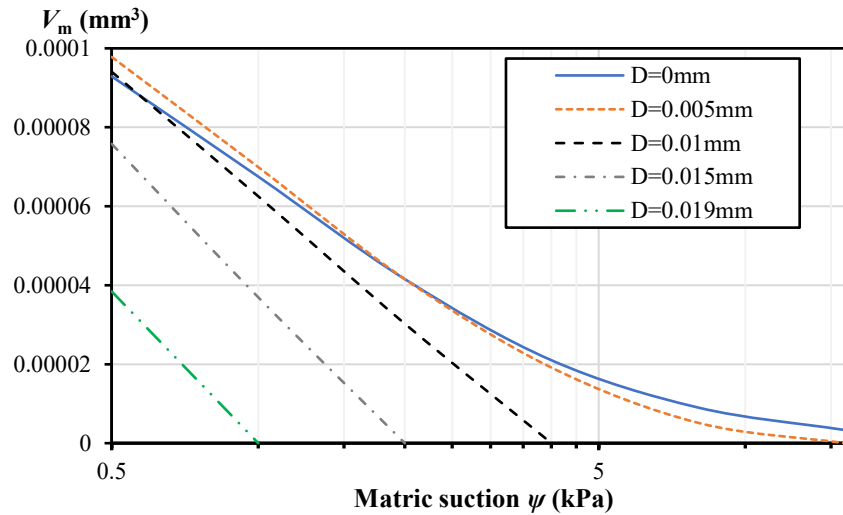
144 The influence of particle size, matric suction, contact angle and inter-particle gap on water
145 content of an unsaturated system was investigated using the abovementioned method, as shown in
146 Figs. 4-6.

147 Fig. 4 shows different water-matric suction curves of three pairs of particles with different
148 particle sizes. It is indicated that particle pairs with larger or unequal sizes tend to have lower
149 values of V_w/V_{sphere} . This suggests that coarser and better-graded granular materials will have lower
150 water content with the same matric suction.



151 **Figure 4. Influence of particle size on the water retention curves of a pair of spheres**
152 **(surface tension $T_s=0.0731$ N/m, contact angle $\beta=0^\circ$, inter-particle gap $D=R_1/2$)**

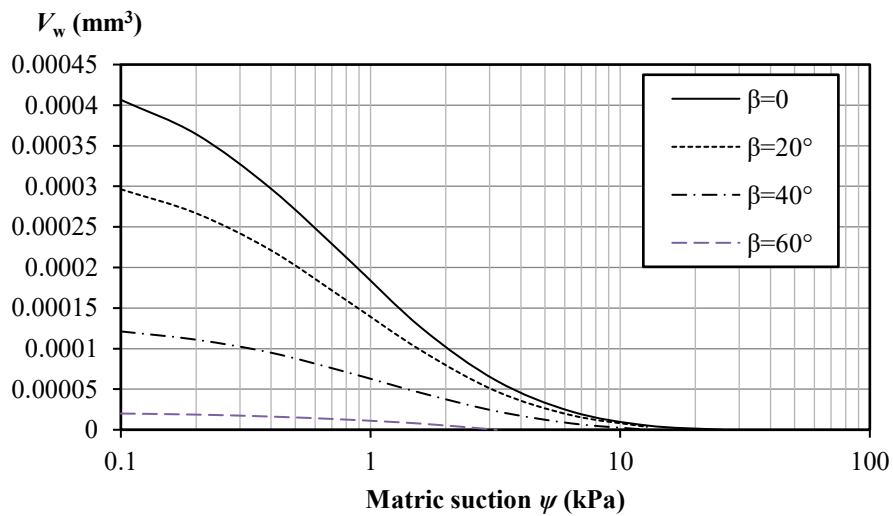
153
154 Fig. 5 shows that for a pair of spheres with 0.1mm diameter, the shape of SWCC is
155 dependent on the values of inter-particle gap D . On general, particles with larger D will have lower
156 water content under the same matric suction. However, when D is very close to zero, the increase
157 of D will cause the SWCC to move up slightly at the lower suction stage. Computation results also
158 show that when D is larger than 0.02mm, no water bridge can be formed between the two particles,
159 indicating the existence of a limit of D for the formation of meniscus toroid.



160 **Figure 5. Influence of inter-particle gap on the water retention curves of a pair of spheres**
 161 ($T_s=0.0731\text{N/m}$, $R_1=R_2=0.1\text{mm}$, $\beta=38.1^\circ$)

162

163 Fig. 6 shows that increasing contact angle results in lower water volume at the level of
 164 matric suction. This effect is one of the possible explanations to the hysteresis phenomenon of
 165 SWCCs during drying and wetting processes in the pendular regime, as the contact angle might be
 166 different in the two processes (Likos and Lu 2004; Gan et al. 2013).



167 **Figure 6. Influence of contact angle on the water retention curves of a pair of spheres**

168 $(T_s=0.0731\text{N/m}, R_1=R_2=0.1\text{mm}, D=0.005\text{mm})$

169

170

171 **2.3 The microscopic model for the funicular regime**

172 The toroidal meniscus model is only applicable for the pendular regime after the residual
173 water content. At the funicular stage, many pores in the granular material are still filled with water.
174 The water can flow in the channels formed by a series of pores, which are usually termed pore
175 throats. A pore throat will transform from saturated to unsaturated state when its pore water shrinks
176 into rings or films after the matric suction increases to a certain value (i.e. snap-off effect) (Likos
177 and Jaafar 2013). The snap-off suction for an idealistic cylindrical throat can be calculated by Eq.
178 12 based on Young-Laplace equation:

$$\psi_s = \frac{2T_s \cos \beta}{r} \quad (12)$$

179 where ψ_s is the snap-off suction and r is the radius of the throat. In granular materials, the
180 size of pore throats is not uniform, which causes different values of ψ_s . In this study, the minimum
181 ψ_s is used as the lower bound of suction (i.e. air entry value, AEV) in funicular regime, as the
182 water begins to flow out from the largest pore throat. Meanwhile, the maximum ψ_s defines the
183 upper bound of suction (i.e. residual suction) in funicular regime, as all pore throats will be
184 unsaturated under this suction value. A straight line was drawn between AEV and residual suction
185 to simulate the funicular regime.

186 In random packing models, it is hard, if possible, to simulate the equivalent radius r and
187 calculate snap-off suction of each three-dimensional pore throat. A simplified process was
188 therefore adopted to determine the snap-off suction of the pore throats within a porous model

189 consisting of randomly packed particles, the details of which will be presented in the subsequent
190 section.

191

192 **3 Simulations of SWCC based on real particle packing**

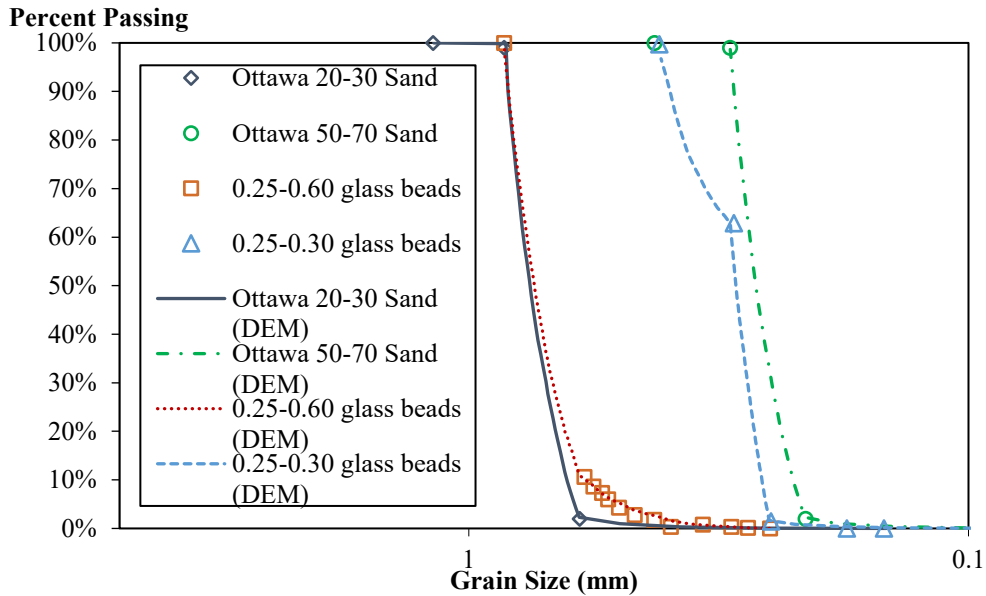
193 **3.1 3D rendition of particle packing with the discrete element method**

194 Packings of several granular material samples reported in the literature (Manahiloh and
195 Meehan 2015; Cao et al. 2017; Jaafar and Likos 2011) were reconstructed with Particle Flow Code
196 (PFC) ^{3D} 5.0 (Itasca 2016). The original porosity (n), D_{50} and grain size distribution are shown in
197 Table 1 and Fig. 7.

198 **Table 1: Measured parameters of granular materials**

Materials	Porosity n	D_{50} (mm)	Sources
Ottawa 20-30 sand	0.417	0.70	Cao et al. 2017
Ottawa 50-70 sand	0.447	0.23	Cao et al. 2017
0.25-0.60 mm glass beads	0.286	0.60	Manahiloh and Meehan 2015
0.25-0.30 mm glass beads	0.375	0.25	Jaafar and Likos 2011

199



200

201 **Figure 7. Grain size distribution of four granular material samples used in the experiments**
 202 **and the simulated results by DEM**

203

204

205

206

207

208

209

210

211

212

213

214

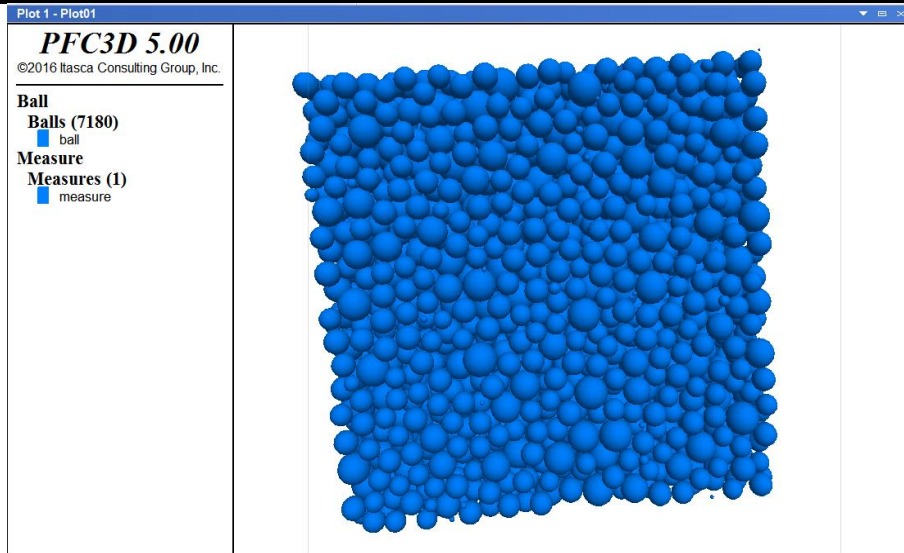
215

216

In the PFC model, granular particles are approximated to be spheres with different radii and distributed randomly in a box under the effect of gravity. Moreover, the Hertz contact model with the approximation theory of Mindlin and Deresiewicz (1953) was employed in this study. Shear modular G and Poisson's Ratio ν are the two most important parameters, which were set as 30 GPa and 0.2, respectively. It was found after the trial and error process that with friction coefficient $\mu = 0.1$, particle overlap can be effectively reduced for glass beads. However, for Ottawa sands with higher porosity, 0.1 was too small to build the models, and therefore 0.5 was used for Ottawa sands. The built PFC model for each type of granular material contained around 4000 to 10000 spheres, distributed in four cubic boxes. It should be noted that the numerical model represents a small soil element instead of the whole soil mass. The parameters of the DEM models are listed in Table 2 and a sample of simulated granular material is shown in Fig. 8. The particle distribution curves of models in PFC are very close to the input ones, as shown in Fig. 7.

Table 2. Parameters of samples in DEM models

Materials	Porosity n	Coordination Number	Friction coefficient μ	Other parameters
Ottawa 20-30 sand	0.417	4.68	0.5	$G=30 \text{ GPa}$
Ottawa 50-70 sand	0.447	5.08		
0.25-0.60 glass beads	0.286	6.55	0.1	$v=0.2$ $\rho=2600 \text{ kg/m}^3$
0.25-0.30 glass beads	0.375	5.61		



217

218 **Figure 8. The numerical model of a typical granular material built in PFC^{3D}**
219

220 **3.2 Construction of SWCC in the pendular regime**

221 The above sections yielded: (1) a meniscus toroid model with accurate numerical solution,
222 which provides a relationship between the meniscus water volume and matric suction at the contact
223 of two spherical particles; and (2) the real packing model of a macroscopic sample consisting of
224 graded spheres, which was rendered with discrete element method at a measured porosity.
225 Combining the above two results, the total meniscus water volume of this sample at a given matric

226 suction which was assumed to be homogeneous within the element (Gras et al. 2011), can be
227 calculated by summing up the volumes of meniscus water between each possible pair of adjacent
228 particles. Thus, the SWCC in the pendular regime can be obtained.

229 Water content can be converted to degree of saturation (S) by Eq. 12:

$$S = V_{\text{water}} / \left(V_{\text{solid}} \cdot \frac{n}{(1-n)} \right) \quad (13)$$

230 **3.3 Construction of SWCC in the funicular regime**

231 A digitized image algorithm was developed on MATLAB to determine the shapes of
232 connected pore throats and to calculate snap-off matric suctions, as elaborated as follows. Firstly,
233 slice the model parallelly into a number of layers along vertical direction, and obtain a binary
234 image for each layer, as shown in Fig. 9. Secondly, identify all independent two-dimensional pores
235 for each layer after smoothing and filtering the images. The snap-off matric suction for each two-
236 dimensional pore is calculated by:

$$\psi_s^{i,k} = \frac{T_s C \cos \beta}{A}, k, i = 1, 2, \dots \quad (14)$$

237 in which A represents the area of the pore, C is the perimeter, i is the pore ID and k is the layer ID.
238 Thirdly, assuming the drainage direction is from the bottom to the top boundary, all 2-D pores at
239 different layers can be connected from the bottom to the top via the overlaps and categorized into
240 a certain number of connected pore throat “trees” in the three-dimensional space. For each
241 connected 3-D pore throat, the snap-off matric suction (ψ_s^i) is controlled by its maximum value
242 within the whole pore throat ($\psi_s^i = \max\{\psi_s^{i,k}\}, k = 1, 2, \dots$). The lower bound of ψ_s^i is the air
243 entry value (AEV) [Eq. (15)], at which the sample begins to desaturate. The upper bound of ψ_s^i

244 corresponds to residual suction (ψ_r) [Eq. (16)] at residual water content, which is the boundary
245 between the funicular and pendular regime, where theoretically there is no saturated pores.

$$AEV = \min\{\psi_s^i\}, i = 1, 2, \dots \quad (15)$$

$$\psi_r = \max\{\psi_s^i\}, i = 1, 2, \dots \quad (16)$$

246 The degree of saturation at AEV is 100%, and the residual saturation degree is calculated
247 by Young-Laplace equation used in the pendular regime. Finally, the SWCC between the two limits
248 is drawn as a straight-line segment to represent the funicular regime, which is a close
249 approximation for coarse-granular materials as the major desaturation process does occur within a
250 very small matric suction range. Thus, the SWCC involving the capillary, funicular, and pendular
251 regimes has been constructed for a granular material sample.

252



(a) Top layer

(a) Middle layer

(c) Bottom layer

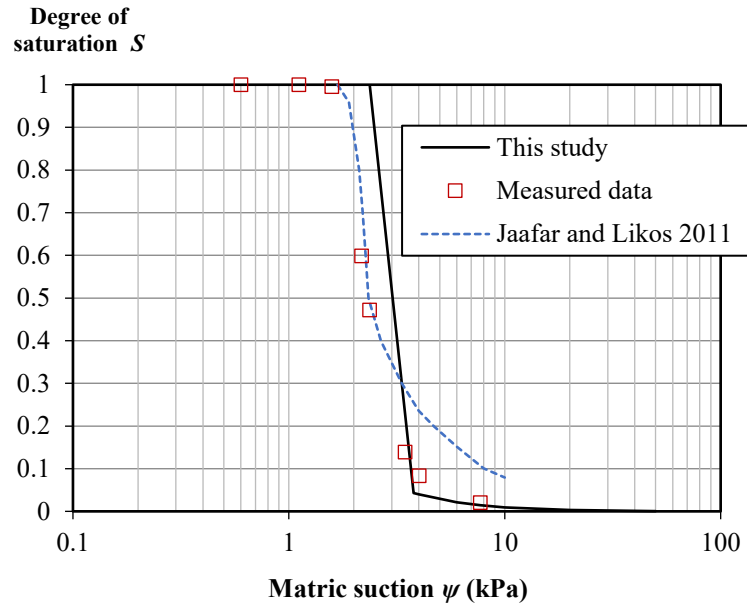
253 **Figure 9. Horizontal cross-sections of the 3-D connected pore throats after smoothing, in**
254 **which the white regions represent the pores and the black regions represent the particles**
255 **(0.25-0.30mm glass beads)**

256

257 **3.4 Results**

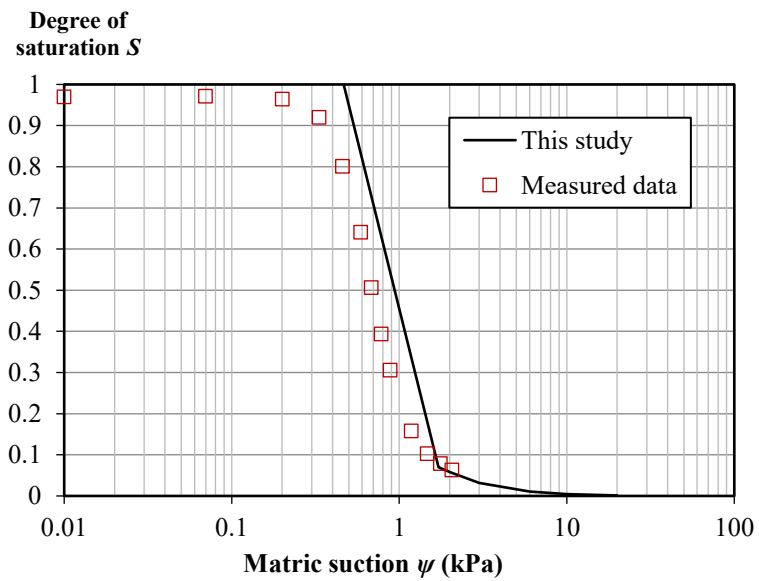
258 Calculated soil water characteristic curves (SWCCs) with the above methods for four
259 granular materials in drying process are shown in Fig. 10. Three features can be identified: (1)
260 Predicted air entry values and residual matric suctions for the four materials were close to
261 measured results; (2) Predicted SWCCs in the funicular regime, *i.e.* a straight-line segment, were
262 similar to the measured curves, which were also close to linear. The exception is that the measured
263 residual degree of saturation of Ottawa 20-30 and 50-70 sands tends to be higher than the predicted
264 values; (3) In the pendular regime, the simulated SWCCs of glass beads agree well with the
265 measured ones, except for very few points where the simulated values were slightly lower. The
266 predicted degree of saturation for both Ottawa 20-30 and 50-70 sands, however, is only a fraction
267 of the measured ones. This phenomenon in the pendular regime is similar to results obtained in
268 previous studies (Likos and Lu 2004; Gras et al. 2011; Suits et al. 2011; Likos and Jaafar 2013).

269 The results by this study are also compared with calculations done by other researchers in
270 the literatures, which demonstrated the strengths of the proposed method. In Fig.10 (a), the
271 calculated SWCC for glass beads captures fits much better at lower saturation than the curve
272 simulated by Jaafar and Likos (2011) using interpolation of idealized packings, while
273 overestimates the suction a bit in funicular regime. For glass beads in Figure.10 (b), the authors
274 did not present any simulation method or results. In Figs.10 (c) and (d), the computed curves in
275 this study approximately fall between the upper bounds and lower bounds by Cao *et al.* (2018), in
276 which ideal packings and circle approximation for meniscus toroid were adopted. The proposed
277 method generally reduced the error in constructions of SWCCs compared to these cited literatures.



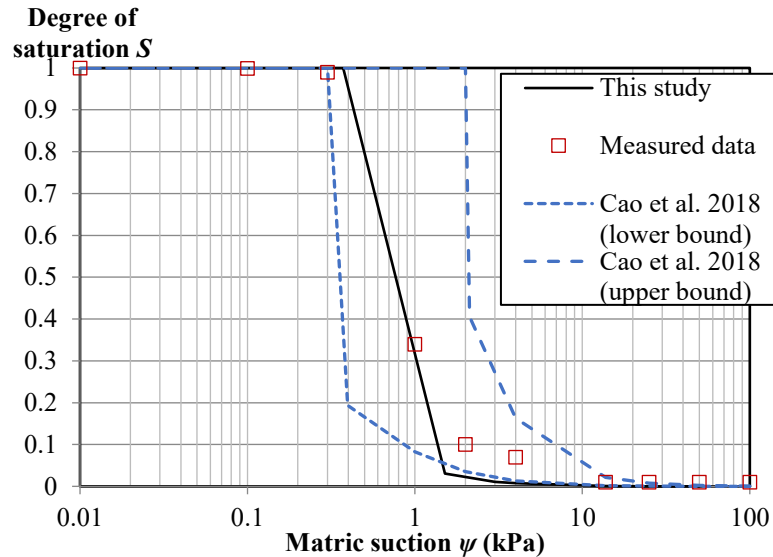
(a) 0.25-0.30 mm glass beads

278



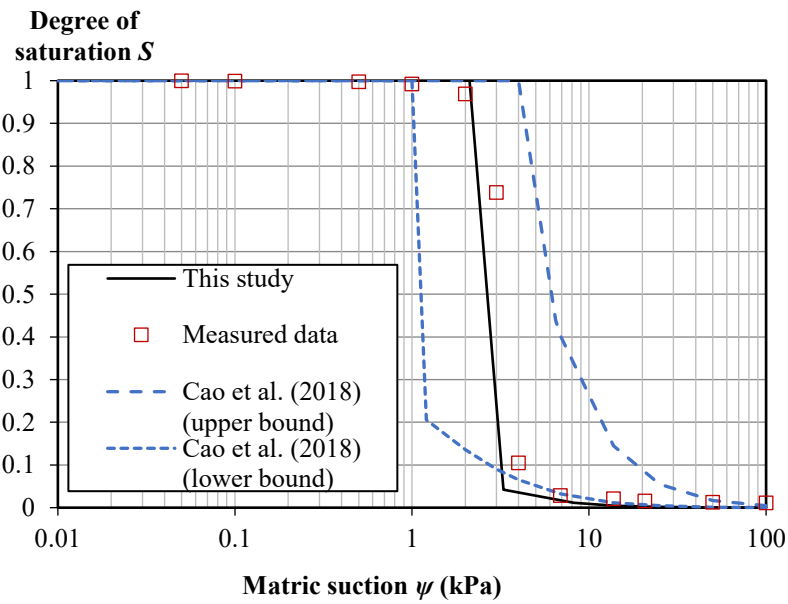
(b) 0.25-0.60 mm glass beads

279



(c) Ottawa 20-30 sand

280



(d) Ottawa 50-70 sand

281 **Figure 10. SWCCs of Ottawa sands and glass beads, in which the solid lines represent the**
 282 **simulated results and the separated points represent the measured data in literatures**

283
284
285

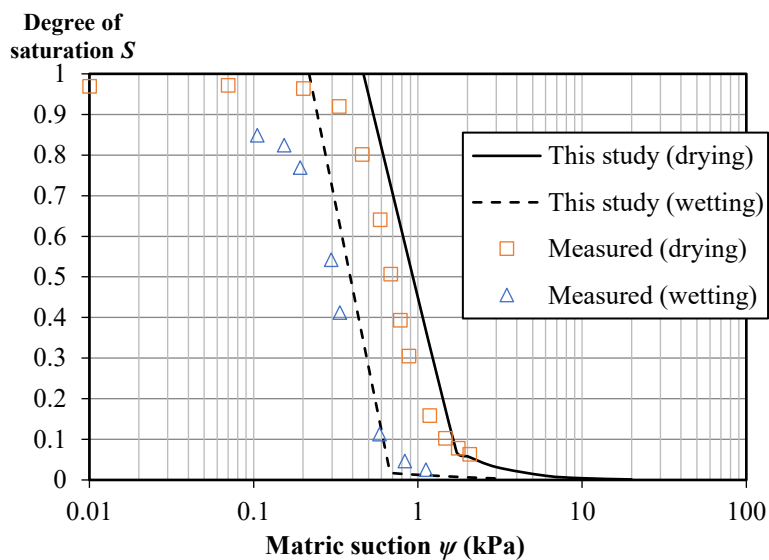
3.5 *Modelling of hysteresis of SWCC in drying and wetting process*

286 Hysteresis phenomenon in drying and wetting is one of the major features of SWCCs for
287 granular materials (Kido et al. 2020; Li et al. 2019; Wen et al. 2020). There are different hypotheses
288 on the hysteresis behaviours of SWCCs, including the ink-bottle effect, which is dominant in high
289 saturation, and the hysteresis of contact angles in drying and wetting process (Likos and Lu 2004;
290 Likos and Jaafar 2013). The ink-bottle is formed in a pore structure with linkage between sections
291 with different diameters. During the drying process, the pore will become desaturate under a higher
292 snap-off suction value, which is controlled by the smaller section at the “bottle neck”. During the
293 wetting process, in contrast, the pore will be saturated under a smaller snap-off suction controlled
294 by the larger section at the body of bottle. Besides, contact angles in wetting process are usually
295 larger than that in drying process. It is revealed in Fig.3 that higher contact angle will generate
296 smaller degree of saturation under the same suction for meniscus toroid.

297 Based on these two mechanisms, the hysteresis of SWCC can be modelled by the following
298 procedures. First of all, modifications can be made on the calculations of funicular regimes
299 presented in Section 3.3 to consider the ink-bottle effect. During the wetting process, the snap-off
300 matric suction (ψ_s^i) for the 3-D pore throat should be controlled by its minimum value within the
301 whole pore throat (*i.e.* $\psi_s^i = \min\{\psi_s^{i,k}\}, k = 1, 2, \dots$), instead of the maximum value. Secondly, a
302 larger value of contact angle should be selected for the wetting process, which is usually between
303 60 to 80 degree (Likos and Lu 2004). Following the above two procedures, the SWCC in wetting
304 process can be simulated.

305 Fig. 11 shows the results for modelling the hysteresis of SWCC for glass beads 0.25-060
306 with comparisons to measured data by Manahiloh and Meehan (2015). The contact angle used for

307 the wetting process is 60 degree. In general, the computed curves fit well with measured ones. For
 308 the wetting process, the results for funicular regime seems better, while the computed residual
 309 saturation is a bit lower than the measured value. The degree of saturation near AEV is assumed
 310 as 100%, which is however overestimated. According to the results of experiments by Manahiloh
 311 and Meehan (2015) and many other researchers, the degree of saturation at AEV is usually smaller
 312 than 100% in wetting process. To properly address this issue, further improvements on the current
 313 method are to be conducted.



314 **Figure 11. SWCCs of glass beads 0.25-0.60 in drying and wetting process, in which the solid**
 315 **316 lines represent the simulated results and the separated points represent the measured data**
in literatures

317

318

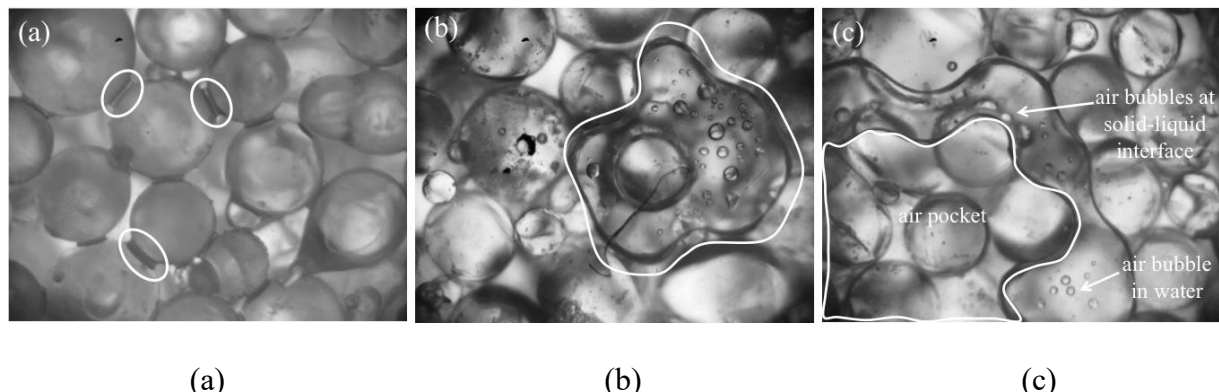
319 **4 Examination by microscopic photos and discussions**

320 **4.1 Microscopic photos of water distribution in an unsaturated granular material**

321 To reveal the distribution of water and air in granular materials, a microscopic photography
 322 experiment was conducted on unsaturated glass beads. Small glass beads with diameters of 0.4-

323 0.6mm were fixed inside a transparent acrylic plate frame and immersed in water before testing.
324 Then the frame was lift above the water level and an unsaturated zone was formed in the glass
325 beads. Due to the capillary effect, the saturation degree inside the material varied with distance
326 from the water level. An industrial camera with magnification lenses was used to take photos of
327 the glass beads and the water therein.

328 Fig. 12 shows three microscopic photos of the glass beads at different height. Where the
329 saturation degree is low, there exists only meniscus toroid [Fig. 12(a)]. However, a high portion of
330 continuous or patchy water inside the pores can be observed where the degree of saturation is high
331 [Fig. 12(b) and (c)]. According to the definition in the previous section, Fig. 12(a) belongs to the
332 pendular regime while (b) and (c) correspond to the funicular regime. The transformation of water
333 phase from saturated state to unsaturated state in (c) and then (a) was considered as the dominant
334 mechanism of the funicular regime in the calculations in this study.



335
336 **Figure 12. Microscopic images of (a) toroid water, (b) patchy water, and (c) complicated**
337 **patterns of air phase, including air pocket, air bubbles in water, and air bubbles in-between**
338 **solid-liquid interfaces**

339
340 **4.2 Limitations of the proposed method**

341 The proposed method is developed based on the micro mechanism of water retention,
342 however, with a series of simplification and assumptions, as revealed in the previous sections. The

343 SWCCs of granular materials predicted with DEM rendition in this study were reasonable for
344 spherical particles (0.25-0.30 mm and 0.25-0.60 mm glass beads), but less reasonable for non-
345 spherical particles (Ottawa 20-30 and 50-70 sands), especially in the pendular regime. There are
346 several reasons contributing to this result, as elaborated in the following paragraphs.

347 (1) In our method, only capillarity effect is considered in this study. Although meniscus
348 toroid and patchy water are the major forms of fluid in the images in Figure 11 for glass
349 beads, it is strongly indicated in some previous studies that adsorbed water exists in
350 granular soils (Leverson and Lohnes 1995; Mason *et al.* 1999). The calculations for
351 adsorbed water have been addressed by different approaches, such as Monte Carlo
352 method in recent studies by Zeidman *et al.* (2016). Discussions on the effect of
353 adsorption and its dependency on materials properties is necessary in further studies to
354 involve the adsorbed water in construction of SWCCs.

355 (2) In the pendular regime, only meniscus toroid water at the particle contacts was
356 considered in the calculation [Fig. 12(a)] and all pore throats were assumed unsaturated
357 (i.e. no patchy water). However, patchy water was observed to be possibly the major
358 water component near the residual water content [Fig. 12(b)], which is discontinuous
359 and cannot be properly simulated by the method in 3.3. In particular, for granular
360 materials with apparent surface roughness or angularity (e.g. Ottawa sand), there will
361 be some smaller pores that cannot be obtained with smooth spheres in the DEM model.
362 According to Eq. (12), smaller pores have higher snap-off suction values to lose water
363 and could be still saturated in the pendular regime. Likos and Jaafar (2013) studied pore
364 water distribution for F-75 sand and postulated that full pores still play a non-ignorable

365 role in the pendular regime. This could be the major reason why the saturation degree
366 of measured SWCCs was higher than the simulated ones after the residual suction.

367 (3) High air entry value ceramic disk based experimental methods (pressure plates, Tempe
368 cell, Fredlund SWCC device) suffer from irreducible saturation at high matric suction
369 due to significantly low hydraulic conductivity in the pendular regime (Likos and Jaafar
370 2013), which leads to rather long equilibrium time (Gee et al. 2002). Indeed, lacking
371 the flow channel for draining this “isolated” water might be another reason for the high
372 measured degree of saturation in the pendular regime measured by this method.

373 (4) Spherical particles were adopted in the presented DEM models for simplicity, which
374 are different from the tested Ottawa sand. Such approximation might have changed the
375 contact numbers, pore sizes and boundary conditions at particle surfaces, and result in
376 errors in calculating water content within the particle packings. Therefore, SWCCs for
377 glass beads with regular shapes and smooth surfaces generally perform better compared
378 to those for Ottawa sand.

379 (5) The method is currently developed coarse granular materials, assuming that both
380 particle geometry and packing remain unchanged during the drying or wetting process.
381 For other materials, such as bentonite soils (Ni *et al.* 2020) with swelling behaviour,
382 the effect of water on the micro behaviours of particles is more complicated. Adsorbed
383 water and meniscus water at pore throats and inter-particle contacts should be analyzed
384 with considerations of the evolutions of particle shape and porosity.

385 Other possible reasons for the differences between simulated and measured SWCCs
386 include the values of contact angle and other complicated patterns of air phase, such as air pocket,
387 air bubbles in water, and air bubbles in-between solid-liquid interfaces [Fig. 12(c)].

388 **5 *Conclusions***

389 The study proposed a new algorithm, which combines microscopic mechanism and discrete
390 element rendition of the real packing of four granular materials to simulate their SWCCs. Packing
391 models of four granular materials (glass beads and Ottawa sands) reported previously were
392 reconstructed with Particle Flow Code (PFC). An improved numerical solution to the Young-
393 Laplace equation, which, by adopting an iteration algorithm to directly reveals the generatrix of
394 the meniscus water, was used to calculate the volume of meniscus water between two adjacent
395 spheres. Upscaling of this improved numerical solution by summing up all the volumes of
396 meniscus water between pairs of adjacent spheres in the packing model rendered by PFC yields
397 the SWCC of the pendular regime. To determine the funicular regime of SWCC, an innovative
398 digitized image algorithm is proposed to obtain the information of connected pore throats in the
399 soil sample. By calculating snap-off suction for these pore throats, the upper and lower bounds for
400 the funicular regime of SWCCs can be determined. The proposed method is also extended to model
401 the hysteresis of SWCCs in drying and wetting process.

402 The simulated SWCCs agree well with the measured ones in general, especially for the
403 AEVs and residual suctions. SWCCs in the pendular regime for glass beads agree better with the
404 measured ones than those for Ottawa sands. Observation of the water distribution pattern with a
405 microscope reveals that patchy water, instead of toroid water, may be the major form of water for
406 fine-grained granular materials. Not considering the adsorbed water and patchy water in the
407 pendular regime is postulated to be the most important factor for the difference. Other possible
408 reasons were also mentioned in this study, including limitations of experimental methods, irregular
409 shapes of natural granular materials, contact angle, etc.

410 Based on the current work, further studies can be conducted to involve patching water,

411 adsorbed water films, irregularly shaped particles in DEM as well as finer irregular particles, such
412 as clayey soils (Ni *et al.* 2020). In addition, shear strength of unsaturated soils is affected by matric
413 suction since the normal stress and cohesion will be influenced by meniscus (Zhai *et al.* 2019).
414 Based on the framework of this study, analysis of shear strength for unsaturated soils can be
415 introduced, by quantifying the effect of surface tension at the meniscus of pore throats and inter-
416 article contacts.

417

418

419 **Acknowledgements**

420 This research was supported by the Ministry of Science and Technology of China (Award No.:
421 2019YFC1805002, 2018YFC1802300), the National Natural Science Foundation of China (Award
422 No.: 51779219), and the Basic Science Center Program for Multiphase Evolution in Hypergravity
423 of the National Natural Science Foundation of China (Award No.: 51988101). Financial support
424 from the Overseas Expertise Introduction Center for Discipline Innovation (B18047) is also
425 acknowledged. The financial support to the first author by the One- Thousand-Young-Talents
426 Program of the Organization Department of the CPC Central Committee and the 100-Talents
427 Program of Zhejiang University is deeply appreciated. Supports from a Theme-based Research
428 Scheme project (T22-502/18-R) and a GRF project (PolyU 152209/17E) from Research Grants
429 Council (RGC) of Hong Kong Special Administrative Region Government of China are also
430 acknowledged. The authors would also like to acknowledge the MOE Key Laboratory of Soft Soils
431 and Geo-environmental Engineering of Zhejiang University and Professor YIN Jian-hua of the
432 Hong Kong Polytechnic University.

433 **Availability of data codes and material**

434 All data, codes and materials generated or used during the study are available from the
435 corresponding author by request.

436 **Conflicts of interest/Competing interests**

437 No conflicts of interests.

438

439 **References**

440 Bittelli, M., and Flury, M. (2009). "Errors in water retention curves determined with pressure
441 plates." *Soil Science Society of America Journal*, 73(5), 1453-1460.

442 Cao, J., Jung, J., Song, X., & Bate, B. (2018). "On the soil water characteristic curves of poorly
443 graded granular materials in aqueous polymer solutions." *Acta Geotechnica*, 13(1), 103-
444 116.

445 Cho, G. C., and Santamarina, J. C. (2001). "Unsaturated particulate materials - Particle-level
446 studies." *Journal of Geotechnical and Geoenvironmental Engineering*, 127(1), 84-96.

447 Duriez, J., and Wan, R. (2017). "Contact angle mechanical influence in wet granular soils." *Acta
448 Geotechnica*, 1-17.

449 Fisher, R. A. (1926). "On the capillary forces in an ideal soil; correction of formulae given by W.
450 B. Haines." *Journal of Agricultural Science*, 16(3), 492-505.

451 Fredlund, D. G. (2006). "Unsaturated soil mechanics in engineering practice." *Journal of
452 Geotechnical and Geoenvironmental Engineering*, 132(3), 286-321.

453 Fredlund, D. G. and Rahardjo, H. (1993). "Soil mechanics for unsaturated soils." *John Wiley &
454 Sons*.

455 Fredlund, D. G., and Xing, A. Q. (1994). "Equations for the soil-water characteristic curve (VOL
456 31, PG 521, 1994)." *Canadian Geotechnical Journal*, 31(6), 1026-1026.

457 Fredlund, D. G., Morgenstern, N. R., and Widger, R. A. (1978). "Shear-strength of unsaturated
458 soils." *Canadian Geotechnical Journal*, 15(3), 313-321.

459 Gan, Y., Maggi, F., Buscarnera, G., & Einav, I. (2013). "A particle–water based model for water
460 retention hysteresis". *Géotechnique Letters*, 3(4), 152-161.

461 Gee, G. W., Ward, A. L., Zhang, Z. F., Campbell, G. S., and Mathison, J. (2002). "The influence
462 of hydraulic non-equilibrium on pressure plate data." *Vadose Zone Journal*, 1(1), 172-178.

463 Gens, A. (1996). Constitutive modelling: application to compacted soils. In *Unsaturated soils*.
464 Edited by E.E. Alonso and P. Delage. Balkema, Rotterdam, the Netherlands. Vol. 3, pp.
465 1179–1200.

466 Gras, J. P., Delenne, J. Y., Soulié, F., and Youssoufi, M. S. E. (2011). "DEM and experimental
467 analysis of the water retention curve in polydisperse granular media." *Powder Technology*,
468 208(2), 296-300.

469 He, W., Zhao, M. H., Chen, Y. G., and Wang, H. H. (2010). "Theoretical study of microscopical
470 mechanisms and computational method of hysteresis in SWCCs." *Rock & Soil Mechanics*,
471 31(4), 1078-1083.

472 Itasca (2016). PFC 5.0 manual, *Itasca Consulting Group Inc.*

473 Kido, R., Higo, Y., Takamura, F., Morishita, R., Khaddour, G., & Salager, S. (2020).

474 Morphological transitions for pore water and pore air during drying and wetting processes
 475 in partially saturated sand. *Acta Geotechnica*, 1-17.

476 Lechman, J., and Lu, N. (2008). "Capillary force and water retention between two uneven-sized
 477 particles." *Journal of Engineering Mechanics*, 134(5), 374-384.

478 Leverson, S. M., and Lohnes, R. A. (1995). "Moisture tension relations in sand." Proc., 1st Int.
 479 Conf. on Unsaturated Soils.

480 Lian, G., Thornton, C., and Adams, M. J. (1993). "A theoretical study of the liquid bridge forces
 481 between two rigid spherical bodies." *Journal of Colloid & Interface Science*, 161(1), 138-
 482 147.

483 Likos, W. J., and Jaafar, R. (2013). "Pore-scale model for water retention and fluid partitioning of
 484 partially saturated granular soil." *Journal of Geotechnical & Geoenvironmental
 485 Engineering*, 139(5), 724-737.

486 Likos, W. J., and Lu, N. (2004). "Hysteresis of capillary stress in unsaturated granular soil."
 487 *Journal of Engineering Mechanics*, 130(6), 646-655.

488 Li, L., Zhang, X., & Li, P. (2019). Evaluating a new method for simultaneous measurement of soil
 489 water retention and shrinkage curves. *Acta Geotechnica*, 14(4), 1021-1035.

490 Lu, N., Kim, T., Sture, S., and Likos, W. J. (2009). "Tensile strength of unsaturated sand." *Journal
 491 of Engineering Mechanics-ASCE*, 135(12), 1410-1419.

492 Lu, N., Lechman, J., and Miller, K. T. (2008). "Experimental Verification of Capillary Force and
 493 Water Retention between Uneven-Sized Spheres." *Journal of Engineering Mechanics*,
 494 134(5), 385-395.

495 Lu, N., Zeidman, B., Willson, C., Lusk, M., and Wu, D.T. (2010) A Monte Carlo paradigm for
 496 capillarity in porous materials. *Geophysical Research Letters*, 37, doi:
 497 10.1029/2010GL045599.

498 Lu, Y. F., Chen, G. F., Luo, X. Q., and Cui, Y. J. (2008). "Study of soil-water characteristical curve
 499 and its influential factors." *Rock & Soil Mechanics*, 29(9), 2481-2486.

500 Manahiloh, K. N., and Meehan, C. L. (2015). "Evolution of interphase contact angle in partially
 501 saturated granular soils using digital analysis of X-Ray computed tomography images." *Geotechnical
 502 Special Publication*, 2092-2101.

503 Mason, T. G., Levine, A. J., Ertas, D., and Halsey, T. C. (1999). "Critical angle of wet sandpiles."
 504 *Physical Review E*, 60(5A), R5044-R5047.

505 Mindlin, R. D., and Deresiewicz, H. (1953). "Elastic spheres in contact under varying oblique
 506 forces." *J. Applied Mech.*, 20(3), 327-344.

507 Mitarai, N. and Nori, F. (2006) Wet granular materials. *Advances in Physics*, 55(1-2):1-45

508 Ni, H., Liu, J., Guo, J., Yang, D., & Chen, Y. (2020). Numerical modelling on water retention and
 509 permeability of compacted GMZ bentonite under free-swelling conditions. *International
 510 Journal for Numerical and Analytical Methods in Geomechanics*, 44(12), 1619-1633.

511 Orr, F. M., Scriven, L. E., and Rivas, A. P. (1975). "Pendular rings between solids: meniscus
 512 properties and capillary force." *Journal of Fluid Mechanics*, 67(4), 723-742.

513 Richefeu, V., Youssoufi, M. S. E., Peyroux, R., and Radjaï, F. (2010). "A model of capillary
 514 cohesion for numerical simulations of 3D polydisperse granular media." *International
 515 Journal for Numerical & Analytical Methods in Geomechanics*, 32(11), 1365-1383.

516 Sheng, D. and Zhou, A.-N. (2010). Coupling hydraulic with mechanical models for unsaturated
 517 soils. *Canadian Geotechnical Journal*, 48:826-840

518 Suits, L. D., Sheahan, T. C., Jaafar, R., and Likos, W. J. (2011). "Estimating water retention
 519 characteristics of sands from grain size distribution using idealized packing conditions."

520 *Geotechnical Testing Journal*, 34(5), 103594.

521 van Genuchten, M. T. (1980). "A closed-form equation for predicting the hydraulic conductivity
522 of unsaturated soils." *Soil Science Society of America Journal*, 44(5), 892-898.

523 Wan, R., Pouragha, M., Eghbalian, M., Duriez, J., & Wong, T. (2019). "A probabilistic approach
524 for computing water retention of particulate systems from statistics of grain size and
525 tessellated pore network". *International Journal for Numerical and Analytical Methods in
526 Geomechanics*, 43(5), 956-973.

527 Zeidman, B. D., Lu, N., & Wu, D. T. (2016). Hysteresis of liquid adsorption in porous media by
528 coarse-grained Monte Carlo with direct experimental validation. *The Journal of Chemical
529 Physics*, 144(17), 174709.

530 Zhai, Q., Rahardjo, H., Satyanaga, A., & Dai, G. (2019). Estimation of unsaturated shear strength
531 from soil–water characteristic curve. *Acta Geotechnica*, 14(6), 1977-1990.

532 Zhang, X., and Lytton, R.L. 2009a. Modified state-surface approach to the study of unsaturated
533 soil behavior. Part I: Basic concept. *Canadian Geotechnical Journal*, 46(5): 536–552.
534 doi:10.1139/T08-136.

535 Zhou, J., and Jian-Lin, Y. U. (2005). "Influences affecting the soil-water characteristic
536 curve". *Journal of Zhejiang University-SCIENCE A*, 6(8), 797-804.